Chinese Chemical Letters 32 (2021) 3753–3761

Contents lists available at ScienceDirect

Chinese Chemical Letters

journal homepage: www.elsevier.com/locate/cclet

Review

Recent advances of vanadium-based cathode materials for zinc-ion batteries

Xuerong Li[a,b,1], Haoyan Cheng[a,1], Hao Hu[a,*], Kunming Pan[a,b,*], Tongtong Yuan[a], Wanting Xia[a]

[a] School of Materials Science and Engineering, Henan University of Science and Technology, Luoyang 471023, China
[b] Henan Key Laboratory of High-temperature Structural and Functional Materials, National Joint Engineering Research Center for Abrasion Control and Molding of Metal Materials, Henan University of Science and Technology, Luoyang 471003, China

ARTICLE INFO

Article history:
Received 16 March 2021
Revised 16 April 2021
Accepted 21 April 2021
Available online 28 April 2021

Keywords:
Aqueous zinc-ion batteries
Vanadium-based materials
Cathodes
Energy storage
Design strategy

ABSTRACT

Zn-ion batteries (ZIBs) have gained great attention as promising next-generation power sources, because of their low cost, enviable safety and high theoretical capacity. Recently, massive researches have been devoted to vanadium-based materials as cathodes in ZIBs, owing to their multiple valence states, competitive gravimetric energy density, but the capacity degradation, sluggish kinetics, low operating voltage hinder further optimization of their performance in ZIBs. This review summarizes recent progress to increase the interlayer spacing, structural stability, and the diffusion ability of the guest Zn ions, including the insertion of different ions, introduction of defects, design of diverse morphologies, the combination of other materials. We also focus on approaches to promoting the valuable performance of vanadium-based cathodes, along with the related ongoing scientific challenges and limitations. Finally, the future perspectives and research directions of vanadium-based aqueous ZIBs are provided.

1. Introduction

The rapid development of electric vehicles and various intelligent devices lead to the huge demand for energy storage devices with high energy density, long-cycle-life, safety and cheap price [1–5]. Among various batteries, alkaline ion batteries (Li^+, Na^+, K^+) are easily standing out because of their ability to provide stable output voltage, which increase the reliability of the equipment operation. Lithium-ion-batteries are most commonly used as commercial rechargeable batteries due to their high energy density and low self-discharge [6–10]. However, potential dangers of electrode materials and the limited lithium resources in the earth crust have made it a challenging task for large-scale applications [11–13]. For sodium-ion batteries, the low operation voltage and the relatively large ionic size of Na^+ lead to sluggish reaction kinetics and poor electrode stability [14]. As for potassium ion batteries, there are severe issues in transport kinetics and cycling stability [15].

Rechargeable aqueous zinc-ion batteries (ZIBs) have been recognized as a promising alternative owing to its merits and advantages: (1) high operational safety [16]; (2) low redox potential of Zn^{2+}/Zn of anode (−0.76 V *vs.* SHE) compared to other anodes in aqueous batteries [17]; (3) high capacity of Zn (820 mAh/g, 5855 mAh/cm^3) [18]; (4) stability in water due to high overpotential for hydrogen evolution [19]. Thus the ZIBs have great potential in the future energy storage field. Due to the low redox potential of Zn and the formation of Zn dendrite, the near-neutral or slightly acidic aqueous electrolyte is more suitable for ZIBs, which may successfully eliminate dendritic Zn deposition prevalent in alkaline electrolytes and further promote the development of ZIBs [20]. To date, various cathode materials in aqueous ZIBs, such as manganese (Mn)-based compound [21], Prussian blue [22], organic material [23], Chevrel phase compound [24] and vanadium-based compound have been developed and gained impressive progress. In short, manganese-based compound electrode materials have been reported in aqueous ZIBs due to the diverse structures and multivalent phases of Mn: +2, +3 and +4 [25–27]. The structure of Mn-based materials usually includes tunnel structure, layered structure and 3D structure, which are built by MnO_6 octahedra sharing corners or edges into chains or tunnels [28–30]. The large interspacing structures allow reversible (de)intercalation of Zn ions [31]. α-MnO_2 is built by the corner-sharing MnO_6 octahedra. During the cycling process, the dissolution of Mn ions in the electrolyte changes the equilibrium of Mn dissolution from the MnO_2

* Corresponding authors.
E-mail addresses: huhao@haust.edu.cn (H. Hu), pankunming2008@haust.edu.cn (K. Pan).
[1] These authors contributed equally to this work.

https://doi.org/10.1016/j.cclet.2021.04.045
1001-8417/

electrode. It means that the irreversible distorted framework reduces the capacity. Prussian blue and its analogues possess a face-centered cubic structure, and the open framework has large channels to allow the rapid diffusion of metal ions [32]. However, the aqueous ZIBs with Prussian blue show poor electrochemical performance [17,20,33]. The structure of organic cathode materials is pinned by weak van der Waals forces. The soft lattice allows molecular reorientation for facile and reversible intercalation of Zn ions with the smallest volume change [34–36]. The Chevrel phase compounds' crystal structure composed of three-dimensional arrays of Mo_6T_8 units can form tridirectional channels consisting of metal ions [24]. This structure can host various cations. But the theoretical capacity of that is very low (129 mAh/g) [37]. Besides, vanadium-based compounds usually present a layered structure consisting of square pyramidal VO_5 units that link each other by sharing edges [38]. Because of the large interlayer spacing, the vanadium-based cathode in aqueous ZIBs has a high Zn ions diffusion rate and valuable specific capacities. However, the problems of sluggish kinetics and capacity degradation of vanadium-based cathode materials must urgently be promoted.

With a focus on the vanadium-based materials for aqueous ZIBs, this article offers a comprehensive review on the development of vanadium-based cathodes with controlled structure for energy storage. We begin with a brief introduction to the reaction mechanism of vanadium-based aqueous ZIBs. We then discuss various strategies involved in interlayer cationic and anions ions, lattice water, as well as devisable oxygen vacancy to increase the lattice spacing to enhance the diffusion rate of Zn ions with desirable capacity and stability, followed by an extensive presentation of diverse morphologies, and combination of other carbon materials to improve electrochemical performance. At the end, we give a brief summary about vanadium-based materials in aqueous ZIBs, together with perspectives on the challenges, opportunities, and new directions for future development. It is hoped this article provides not only a comprehensive review of the vanadium-based cathodes in aqueous ZIBs but also the necessary knowledge to push their commercial application.

2. Reaction mechanism of vanadium-based aqueous ZIBs

The charge and discharge process of vanadium-based aqueous ZIBs is the insertion/extraction of hydrous Zn ions into/from their hosts. For many kinds of cathode materials, interlayer ions ($M_xV_nO_m$, M = inserted ions or structural water) were acted as pillars to improve structural stability during the insertion/extraction of Zn ions into the layered oxide. As shown in Fig. 1, for the discharge process, the negative electrode undergoes an oxidation reaction to generate Zn ions, which diffuses to the electrolyte and intercalate into the vanadium oxide layer. Usually, the hydrous Zn ions combine with six water molecules and co-insert into the vanadium oxide layer, which can easily destroy the host structure [39]. For instance, the discharge process in the first cycling reaction of V_2O_5 is as follows:

$$M_xV_nO_m + yZn^{2+} + 2ye^- \rightarrow Zn_yM_xV_2O_5 \quad (1)$$

For the subsequent charge process, the Zn ions between V_2O_5 layers extract and move to the anodewith the electrolyte. The reaction is as follows:

$$Zn_yM_xV_2O_5 \rightarrow Zn_pM_xV_2O_5 + (y-p)Zn^{2+} + (x-q)M^{n+} + (2y-np)e^- \quad (2)$$

Various layered frameworks of vanadium-based compounds are linked by sharing corners/edges polyhedron, with structural water acted as pillars between the layers. For instance, the V_2O_5 layers are built by VO_6, VO_5 and VO_4 polyhedron [40]. The water-based shield formed by structural water reduces the "effective charge" of Zn ions, and increases the distance between Zn ions and the neighboring oxygen-ions in VO_x polyhedron, resulting in the lower diffusion coefficient [41]. During the charge/discharge process, the phase transformation companied by solid-solution behavior can be observed during the (de)intercalation of Zn ions. During discharging, a new phase occurs when the Zn ions intercalate into vanadium oxide, followed by the transformation to the original state during charging [42]. The more completely the cathode transforms, the more reversible the host structure is, which means the cathode has excellent electrochemical performance. Sometimes the formation of the irreversible byproduct, such as $ZnSO_4Zn_3(OH)_6{\cdot}5H_2O$, can prevent the (de)intercalation of Zn ions, leading to the failure of battery at last [43].

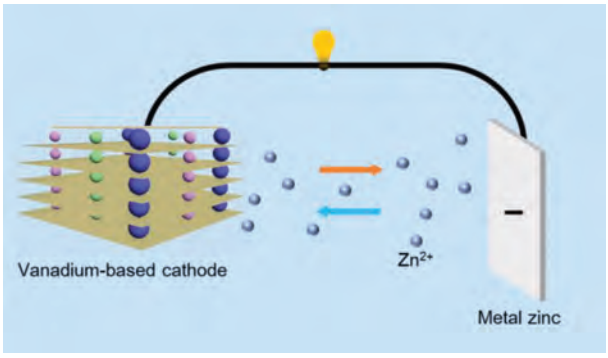

Fig. 1. Reaction mechanism of vanadium-based aqueous ZIBs.

3. Vanadium-based compound with interlayer cationic ions

3.1. Vanadium-based compound with interlayer monovalent cations

Vanadium-based compounds with interlayer monovalent cations as cathodes have been studied for years. Yang *et al.* introduced an effective strategy by the chemical intercalation of Li ions into the interlayer of $V_2O_5{\cdot}nH_2O$, with enlarged layered spacing (Fig. 2a) [44]. The Ganlvanostatic Intermittent Titration Technique (GITT) in Fig. 2b reflected a high diffusion coefficient, which benefited from the chemical intercalation of Li ions, enlarging the interlayer spacing. The obtained materials presented a discharge capacity of 232 mAh/g after 500 cycles at 5 A/g. He's group prepared $Na_{0.33}V_2O_5$ nanowires with Na^+ intercalating between the layers of $[V_4O_{12}]_n$ (Figs. 2c and d) [45]. The Na ions not only improved the stability of the tunnel structure as pillars during the insertion/extraction of Zn ions, but also enhanced the conductivity of V_2O_5. The obtained $Na_{0.33}V_2O_5$ electrode delivered reversible intercalation reaction mechanism (Fig. 2e) and high capacity as well as long-term cyclic stability with a capacity retention over 93% for 1000 cycles. Hu *et al.* [46] prepared $Na_2V_6O_{16}{\cdot}1.63H_2O$ nanowires and studied the influence of crystalline water on the properties of materials. They certified that crystalline water played an important role in the electrochemical properties of $Na_2V_6O_{16}{\cdot}1.63H_2O$ cathode materials, which might increase the capacity and improve the stability of the materials. In addition, the other research work about $Na_2V_6O_{16}{\cdot}2.14H_2O$ nanobelts [47] also showed a high capacity of 438 mAh/g at the rate of 0.1 A/g. Du *et al.* [48] synthesized Mn-doped $NaV_8O_{20}{\cdot}nH_2O$ nanobelts *via* one-step hydrothermal method. They found the co-insertion of Na ions and Mn ions enlarged the interlayer spacing, resulting in the stable structure and excellent electrochemical performance.

In recent work, $K_{0.5}V_2O_5$ cathode was prepared by intercalating of K ions into V_2O_5, constructing a stable crystal structure by forming chemical bonds between V_2O_5 layers. The obtained $K_{0.5}V_2O_5$

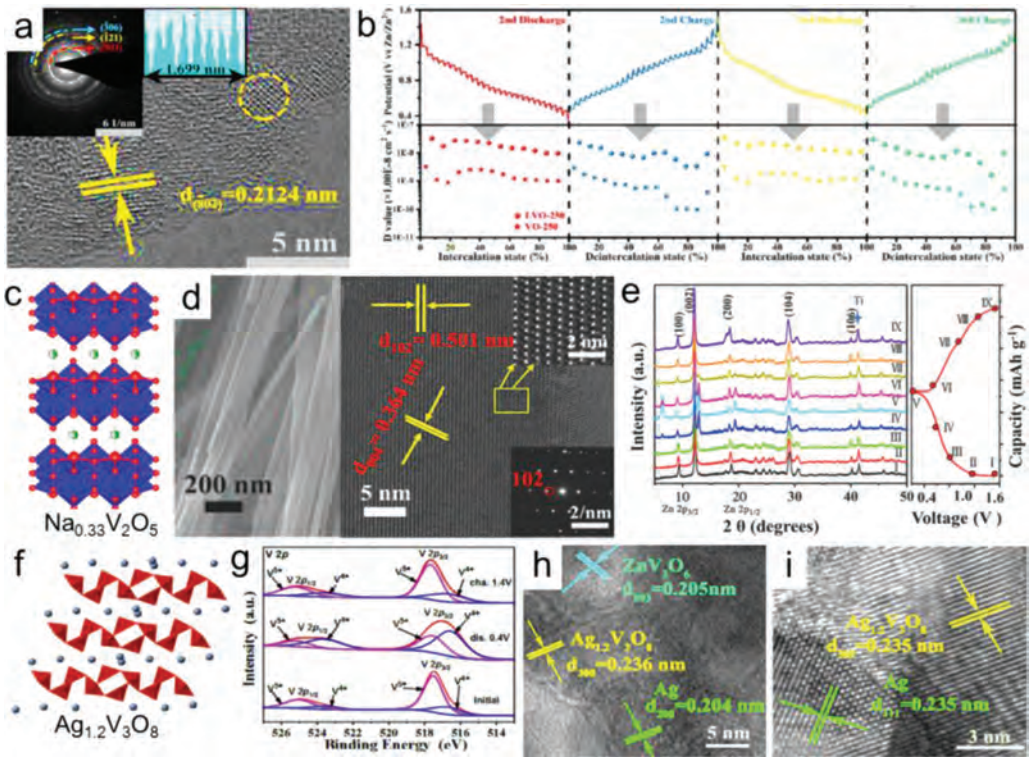

Fig. 2. (a) The HRTEM image with SAED pattern of $Li_xV_2O_5$•nH_2O at 0.1 A/g. (b) The discharge/charge curves in GITT measurement of $Li_xV_2O_5$–250 and the corresponding diffusivity coefficient (D) of Zn ion in the discharge and charge processes of the $Li_xV_2O_5$–250 and V_2O_5–250. Copied with permission [44]. Copyright 2018, the Royal Society of Chemistry. (c) The crystal structure, (d) SEM, HRTEM and (e) *ex situ* XRD patterns of $Na_{0.33}V_2O_5$. Copied with permission [45]. Copyright 2018, Wiley-VCH. (f) The crystal structure, (g) XPS spectra, (h) HRTEM and (i) TEM images of $Ag_{1.2}V_3O_8$. Copied with permission [54]. Copyright 2019, Elsevier.

electrode exhibited excellent durability [49]. The K-O bonds stabilized the structure which liked the pillars and slowed down the dissolution process of V element from V_2O_5. The insertion of K ions led to the reduced lattice space due to the enhancement of attraction between K and O ions. The smaller lattice space might inhibit the intercalation of K ions into V_2O_5 layers. In another research work, $K_{0.23}V_2O_5$ with tunnel structure had been prepared by hydrothermal method and employed as cathode material for aqueous ZIBs, in which, K ions also acted as pillars between the V_2O_5 layers [50]. This material delivered excellent structural stability and high capacity retention rate of 92.8%. It could remain 92.8% of original capacity after 500 cycles at the rate of 2 A/g. $K_2V_8O_{21}$ and $K_{0.25}V_2O_5$ with tunnel structure also has stable structures [51]. The pre-intercalation of potassium ions still enlarged the interspacing of V_2O_5. $K_{0.486}V_2O_5$ as cathodes in aqueous ZIBs showed a large interlayer spacing of 0.95 nm, which was much larger than that of V_2O_5 (0.436 nm) [52]. The advantage of structures ensured reversible Zn ions insertion/extraction. Another work evidenced that K ions intercalated V_2O_5 nanorods with exposed layered structure provided facile access for guest ions to intercalation/deintercalation into/from structure, which led to better performance: discharge capacities of 439 and 286 mAh/g at current densities of 50 and 3000 mA/g [53].

Owing to unique electrical properties and high specific capacity, silver vanadates, in which two types of redox metal centers existed, showed great potential as cathode materials in energy storage devices. A series of Ag ions doped vanadium-based oxides with different structure and Ag content was used in aqueous ZIBs, for example, $Ag_{0.33}V_2O_5$ with a rigid three dimensional tunneled structure, $Ag_{1.2}V_3O_8$, $Ag_2V_4O_{11}$ with a typical layered structure, β-$AgVO_3$ with chain-like structure and $Ag_4V_2O_7$ with island-like structure [54]. The ratio of Ag/V played an important role in structure and electrochemical behaviors. For $Ag_{1.2}V_3O_8$, Ag^0 nanoparticles would be generated upon Zn ions intercalation process and were largely reversible oxidized to Ag ions upon Zn ions de-intercalation process, showing highly structural and cycle stability. The V(V) was reduced to V(IV) and turned back to the original state during the reaction progress, which demonstrated the highly reversibility (Figs. 2f and g). Since the *in-situ* generation of highly conductive Ag^0 and their grid structures, $Ag_{1.2}V_3O_8$ and $Ag_2V_4O_{11}$ with moderate Ag/V ratio presented good rate performance. Some Ag^0 particles could be observed on $Ag_{1.2}V_3O_8$ nanorod during discharging (Fig. 2h), and still existed in the fully charged state (Fig. 2i), which could contribute the significant increase of electronic conductivity and rate capacity. Shan's group revealed the combination displacement/intercalation (CDI) reaction in $Zn/Ag_{0.4}V_2O_5$ system [55]. They found that the characteristic peaks of $Zn_2(V_3O_8)_2$ in XRD spectra became stronger during discharging process and disappeared during the charging process, demonstrating the Zn^{2+}/Ag^+ displacement reaction occurred during Zn ions insertion/extraction in the $Ag_{0.4}V_2O_5$ structure. The Zn ions intercalated into $Ag_{0.4}V_2O_5$ and replaced the Ag ions sites, while Ag ions were reduced to metallic Ag^0. The reaction mechanism offered $Ag_{0.4}V_2O_5$ a rigid structure and good electrochemical properties.

Ammonium vanadate presented a similar structure with other vanadium-based compounds. The existence of hydrogen bonds between ammonium ions and V_2O_5 layer offered a more stable layer structure [56]. $(NH_4)_2V_6O_{16}$ nanobelts showed a high capacity of 323.5 mAh/g at 2.4 A/g and a long cycle performance of 78.3% retention after 2000 cycles at 5 A/g [57]. $(NH_4)_2V_6O_{16}$•$1.5H_2O$ nanobelts showed better cycling performance because the hydrated ammonium ions acted as pillars to stabilize the structure. At the current density of 3 A/g, the capacity of 209.6 mAh/g after 1000 cycles could be obtained. Both T. Wei *et al.* [58] and B. Tang *et al.* [59] demonstrated the ammo-

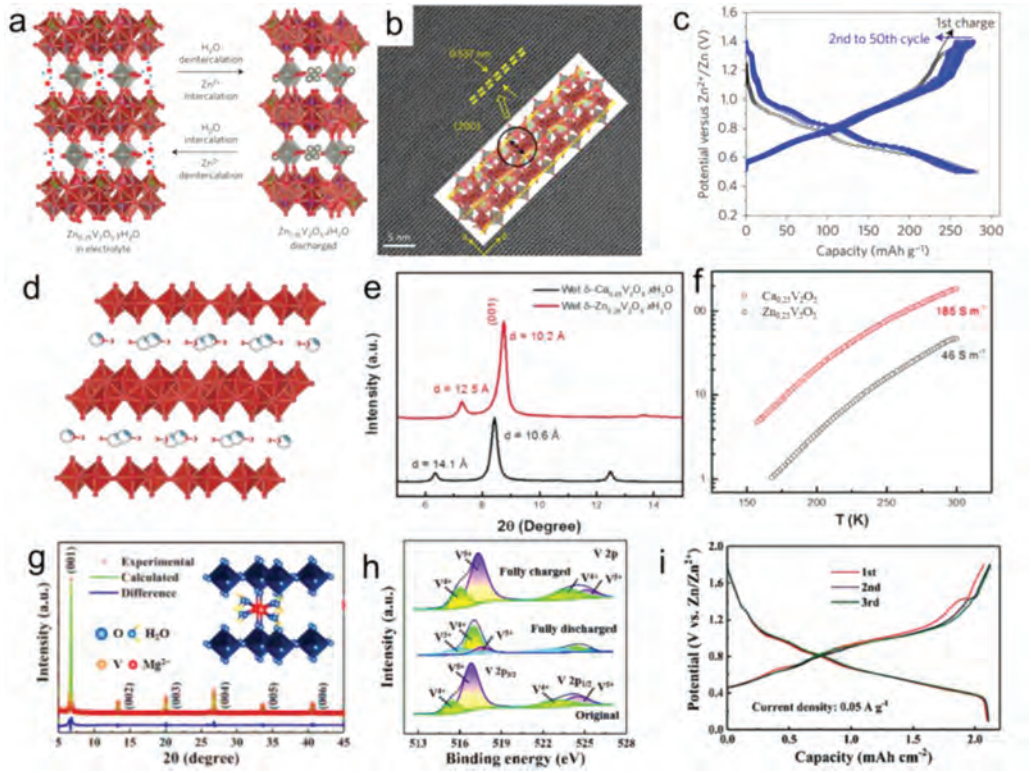

Fig. 3. (a) The structure analysis, (b) HRTEM image and (c) galvanostatic discharge and charge profiles of $Zn_{0.25}V_2O_5{\bullet}H_2O$. Copied with permission [60]. Copyright 2016, Springer Nature. (d) The crystal structure, (e) XRD pattern and (f) electricity conductivities of $Ca_{0.25}V_2O_5{\bullet}xH_2O$. Copied with permission [61]. Copyright 2017, Wiley-VCH. (g) The XRD pattern, (h) XPS spectra and (i) charge/discharge curves of $Mg_{0.26}V_2O_5{\bullet}0.73H_2O$. Copied with permission [65]. Copyright 2020, Wiley-VCH.

nium ions and crystal water molecules stabilized the structure. Zhao *et al.* [39] synthesized $(NH_4)_{0.58}V_2O_5{\bullet}0.98H_2O$ and revealed the Zn ions storage mechanism. The large interlayer distance of 10.9 Å in $(NH_4)_{0.58}V_2O_5{\bullet}0.98H_2O$ meant more Zn ions could be de/intercalated into V_2O_5 layers and this structure allowed more $[Zn(H_2O)_6]^{2+}$ to insert into V_2O_5 layers. When the interlayer could not accommodate more $[Zn(H_2O)_6]^{2+}$, $[Zn(H_2O)_6]^{2+}$started to dehydrate as Zn ions and water molecules, and the formed Zn ions intercalated into V_2O_5 layers. With the deeply discharging, the formation of $ZnSO_4Zn_3(OH)_6{\bullet}5H_2O$ byproduct accelerated the desolvation of $[Zn(H_2O)_6]^{2+}$ into Zn ions. The Zn ions with small radius were more easily inserted into V_2O_5 layers. The charging progress was fully reversible. The inserted cations not only enlarge the interlayer spacing to accommodate more Zn ions for high capacity, but also stabilize the host structure by bond force.

3.2. Vanadium-based compound with interlayer divalent cations

Vanadium oxide bronze pillared by interlayer Zn ions can lead to more than one Zn ion per formula unit during reversible Zn ions (de)intercalation storage process, thus showed high capacity. L. F. Nazar *et al.* [60] prepared $Zn_{0.25}V_2O_5{\bullet}H_2O$ with excellent layered structure by microwave hydrothermal method. As shown in Fig. 3a, the ZnO_6 octahedron was arranged in order in the layered V_2O_5, which supported the V_2O_5 layers and expanded the channel for the insertion/extraction of Zn ions as pillars. In addition, this excellent layered structure enabled water molecules in the electrolyte to be intercalated into V_2O_5 layers, further increasing the layer distance of V_2O_5 (Fig. 3b). During charging and discharging, V_2O_5 layer space could reach 12.9 Å. The obtained materials presented a high capacity of 282 mA/g at 0.3 A/g (Fig. 3c). Compared to $Zn_{0.25}V_2O_5{\bullet}nH_2O$, the double-layered calcium vanadium oxide bronze ($Ca_{0.25}V_2O_5{\bullet}nH_2O$) was more suitable for aqueous ZIB intercalation cathode because the larger CaO_7 polyhedra in $Ca_{0.25}V_2O_5{\bullet}nH_2O$ may further expand the cavity size between V_4O_{10} layers. The structure of $Ca_{0.25}V_2O_5{\bullet}xH_2O$ was shown in Fig. 3d, with a length of Ca-O bond of 2.38–2.57 Å [61], which was longer than the length of Zn-O bond (2.03–2.13 Å) in δ-$Zn_{0.25}V_2O_5{\bullet}xH_2O$. The interlayer space of $Ca_{0.25}V_2O_5{\bullet}nH_2O$ increased from 10.6 Å to 14.1 Å after the insertion of water molecules from the electrolyte into its interlayer space (Fig. 3e). The $Ca_{0.25}V_2O_5{\bullet}nH_2O$ offered 4-folds higher electrical conductivity than $Zn_{0.25}V_2O_5{\bullet}nH_2O$ nanobelt (Fig. 3f), which could boost the electron transfer during Zn ion (de)intercalation, thereby enhancing battery performance.

In addition, the recent research showed that $Ca_{0.23}V_2O_5{\bullet}0.95H_2O$ nanobelt with a large interlayer spacing of 13.0 Å also had high capacity (355.2 mAh/g at 0.2 A/g) and excellent cycling performance (97.7% capacity retention over 2000 cycles at 5 A/g) [62]. Patridge *et al.* [63] studied the changes of the local structure of $Ca_xV_2O_5{\bullet}xH_2O$ during the intercalation of Zn ions and the impacts on cycling performance. They proved that $Ca_xV_2O_5{\bullet}xH_2O$ was a promising cathode for the future storage device. Ming's group [64] prepared the $Mg_{0.34}V_2O_5{\bullet}nH_2O$ nanobelts. After magnesium ions and crystalline water were inserted into the V_2O_5 layer, the distance of the V_2O_5 layer was achieved to 13.4 Å, which resulted in a fast diffusion coefficient of Zn ions and good rate performance. This material also presented excellent cycling performance. At the current density of 5000 mA/g, 97% of the initial capacity was maintained after 2000 cycles. Wang *et al.* [65] studied the advantages of the intercalation of hydrated Zn ions into $Mg_{0.26}V_2O_5{\bullet}0.73H_2O$. The XRD pattern of $Mg_{0.26}V_2O_5{\bullet}0.73H_2O$ and the Rietveld refinement result are shown in Fig. 3g. Mg ions improved the interlayer spacing by acting as pillars, and the larger interlayer space allowed more incorporated Zn cations with six water molecules to insert, which

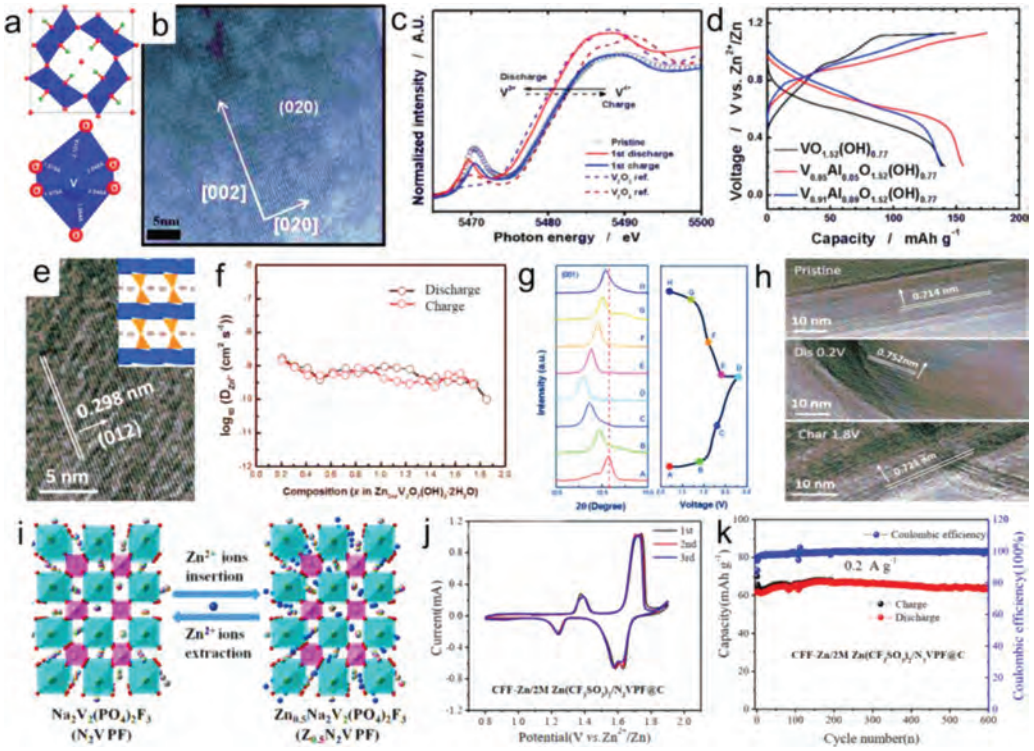

Fig. 4. (a) The model structure, (b) HRTEM image and (c) K-edge XANES spectra of $V_{1-x}Al_xO_{1.52}(OH)_{0.77}$. (d) First discharge–charge curves of $VO_{1.52}(OH)_{0.77}$, $V_{0.95}Al_{0.05}O_{1.52}(OH)_{0.77}$ and $V_{0.95}Al_{0.05}O_{1.52}(OH)_{0.77}$. Copied with permission [72]. Copyright 2017, the Royal Society of Chemistry. (e) HRTEM image, (f) the corresponding Zn ions coefficients, (g) *ex situ* XRD patterns of $Zn_3V_2O_7(OH)_2{\cdot}2H_2O$. (h) HRTEM of the $Zn_3V_2O_7(OH)_2{\cdot}2H_2O$ at initial, fully discharged (0.2 V) and charged (1.8 V) state. Copied with permission [73]. Copyright 2017, Wiley-VCH. (i) Zn storage mechanism illustrations, (j) CV curves and (k) initial three charge/discharge profiles of $Na_3V_2(PO_4)_2F_3$. Copied with permission [80]. Copyright 2018, Elsevier.

required lower intercalation energy. The reversible electrochemical reduction can be discovered in the V 2p XPS region (Fig. 3h). The co-inserted water molecules could shield the effective charge of Zn ions, which increased the diffusion coefficient of Zn ions, leading to a high capacity of 212 mAh/cm^2 at 0.05 A/g (Fig. 3i).

Liu *et al.* [66] prepared manganese expanded hydrated vanadate with high stability, in which, the Mn(II) cations acted as structural pillars, expanded the interplanar spacing, connected the adjacent layers, and partially translated pentavalent vanadium cations to tetravalent. They found that the expanded interplanar space of 12.9 Å reduced electrostatic interactions. And transition metal cations collectively catalyzed more Zn ions intercalation at higher discharge current densities with enhanced reversibility and cycling stability. Li *et al.* prepared δ-$Ni_{0.25}V_2O_5{\cdot}nH_2O$ that Ni ions coordinated two oxygen ions, which led to more apical oxygen ions in V_2O_5 layers [67]. The oxygen ions made Zn ions easier to intercalate. And the structure with double layers was stable. In addition, other transition metal ions (Fe, Co, Ni, Mn, Zn, Cu) doped vanadate system could also improve the capacity by enlarging interlayer spacing and stabilized the structure [68]. These cathodes showed good cycling performance even in a range of testing temperatures (0–50 °C).

Intercalating copper-ions produced another electrochemical mechanism that reduction displacement reaction occurred during the discharge process [69]. After Zn ions being intercalated into the cathode material, Cu ions were reduced to Cu^0 nanoparticles, then parts of Cu^0 nanoparticles were oxidized to Cu ions charging. This process promoted multiple electron transfer and increased battery capacity. CuV_2O_6 nanowires prepared by Yu *et al.* [70] proved that the multistep reduction reactions of Cu ions and V ions with the intercalation of Zn ions provided high capacity (338 mA/g at 0.1 A/g). In another research, Liu *et al.* [71] prepared CuV_2O_6 nanobelts and found that the displacement between Zn and Cu was reversible and would not damage the VO_6-octahedron chains.

3.3. Vanadium-based compound with both interlayer cations and anions

In typical hollandite-type vanadium oxide, the hydrogen atoms attached to the edge-sharing oxygen atoms of oxide ions in the channels to form OH groups, resulting in highly stable structure. Jo *et al.* [72] synthesized $V_{1-x}Al_xO_{1.52}(OH)_{0.77}$ by a solvothermal synthesis method. As shown in Fig. 4a, the distorted VO_6 octahedra shared an edge to form VO_6 double chains, and there was an oxygen ion in the tunnel. This tunnel-type structure had a larger space to accommodate more ions (Fig. 4b). The X-ray absorption near edge structure (XANES) spectroscopy data indicated successful doping of Al into the hollandite $VO_{1.52}(OH)_{0.77}$ tunnel structure (Fig. 4c). The Al-O bond strongly stabilized the structure, resulting in better electrochemical properties compared with Al-free $VO_{1.52}(OH)_{0.77}$ (Fig. 4d). $Zn_3V_2O_7(OH)_2{\cdot}2H_2O$ also had a tunnel-type structure that was composed of zinc oxide layers separated by $V_2O_7^{4-}$ groups (Fig. 4e) [73]. The open-framework structure allowed fast Zn ions migration and better performance (Fig. 4f). The reversible interlayer expansion could be observed due to the stable structure (Figs. 4g and h). $Cu_3V_2O_7(OH)_2{\cdot}2H_2O$ [74] had a structure that was built up of $Cu_3O_6(OH)_2$ layers separated by V_2O_7 pillars and water molecules. During the discharging process, Cu^0 formed and the metallic Cu^0 had not been oxidized at the initial stage of charging, which resulted in high electrical conductivity, fast electron transfer, and rapid extraction of Zn ions. Peng and coworkers [75] prepared $Fe_5V_{15}O_{39}(OH)_9{\cdot}9H_2O$ nanosheets with a high capacity of 385 mAh/g at 0.1 A/g. During discharging and the insertion of Zn ions, V^{5+} was reduced to V^{4+} and V^{3+}, and the concomitant

oxidation of Fe^{3+} to Fe^{2+}. Both Fe and V were electrochemical active for Zn storage mechanism.

Additionally, the vanadium-based compound with polyanionic has been reported as cathode for aqueous ZIBs. Many groups showed interest on NASICON $A_xMM'Z(XO_4)_3$ (A = Li, Na, Mg, *etc.*; M, M' = Ti, V, Cr, Fe, *etc.*; X = P, Si, S, *etc.*) compounds [76]. $(PO_4)^{3-}$ polyanion could moderate the energy of the transition metal redox couple to generate relatively high operating potentials and the strong covalent units could provide structural stability even at high charge states and address thermal safety concerns [77]. $Na_3V_2(PO_4)_3$ also had a layer framework [78]. And there were two Na sites with different coordination environments, one of which could be extracted from $Na_3V_2(PO_4)_3$ to electrolyte with the transformation of $Na_3V_2(PO_4)_3$ into $NaV_2(PO_4)_3$ during the charging process. The other Na site provided a large open site that could accommodate the other four Na ions. During discharging, Zn ions achieved reduction reaction, and Na ions were inserted into $NaV_2(PO_4)_3$ to form back $Na_3V_2(PO_4)_3$. In the monoclinic $Li_3V_2(PO_4)_3$ cathodes, the $(PO_4)^{3-}$ polyanions facilitated to form three dimensional pathway for Li ions insertion/extraction with a very high Li-ion diffusion coefficient (from 10^{-9} cm/s to 10^{-10} cm/s) [79]. The three pairs of redox peaks revealed the two-lithium-ion de/intercalation behaviors. $Li_3V_2(PO_4)_3$ showed stable cycle performance that the capacity retention was 85.4% after 200 cycles at 0.2 C. Due to the strong affinity of F atoms toward the surroundings, $Na_3V_2(PO_4)_2F_3$ showed a more stable structure than $Na_3V_2(PO_4)_3$ [80]. As shown in Fig. 4i, the framework of $Na_3V_2(PO_4)_2F_3$ provided more convenient pathways for the insertion/extraction of Zn ions. The initially cathodic scan corresponds to the extraction of Na ions from Na(2) sites and the anodic scan corresponds to the insertion of Zn ions (Fig. 4j). And $Na_3V_2(PO_4)_2F_3$ showed good cycling performance due to the facile diffusion of H ions into the host structure (Fig. 4k). $Na_3V_2(PO_4)_2O_{1.6}F_{1.4}$ [81] exhibited a high operation potential of ~1.46 V and good electrochemical performance. The polyanions can help generate a three-dimensional framework and abundant large vacancies, which leads to promising electrochemical performance.

In general, the inserted cations and anions not only strengthen atomics force and change the valence states to enhance the conductivity of vanadium-based cathodes, but also promote water molecular to intercalate into the interlayer, leading to the enlarged lattice spacing and increased capacity.

4. Oxygen vacancy in vanadium compound

V_3O_7 is a typical low-valent vanadium compound with oxygen vacancy. Kundu *et al.* [82] prepared layered $V_3O_7{\cdot}H_2O$ that connected by hydrogen bonds, which was composed of VO_6 octahedra and VO_5 trigonal bipyramids. The hydrogen bonds strongly stabilized the structure compared with other vanadium compounds that were combined by Van der Waals force between layers. $V_3O_7{\cdot}H_2O$ showed a high capacity of 400 mAh/g at 375 mA/g and small charge transfer resistance of 20 Ω, manifesting fast interface kinetics. Crystalline water is also crucial to the property of V_3O_7. Wang *et al.* [83] compared the properties between $V_3O_7{\cdot}H_2O$ and V_3O_7. $V_3O_7{\cdot}H_2O$ presented higher capacity, meaning that crystalline water maintained the layer structure for the (de)intercalation of Zn ions. Pang *et al.* [84] synthesized $H_2V_3O_8$/graphene *via* a one step hydrothermal method (Fig. 5a). The vacancy sites between V–O octahedrons could accommodate the intercalation of Zn ions (Fig. 5b), leading to a high capacity of 394 mAh/g at 1 C rate (Fig. 5c). V_6O_{13} with alternative single/double layers showed high capacity and good long-term cyclability [85]. Different from other previously reported Zn ions storage mechanisms, a highly reversible phase of $Zn_{0.25}V_2O_5{\cdot}H_2O$ appeared during discharging and disappeared during charging. The phase of $Zn_{0.25}V_2O_5{\cdot}H_2O$ not only stabilized the structure, but also produced more phase boundaries, resulting in more active sites, which was conducive to numerous Zn ions storage. Shin *et al.* [86] further studied the electrochemical mechanism of V_6O_{13} nanosheeets/Zn system, the morphology was shown in Fig. 5d. They found that co-intercalated water could shield electrostatic interactions with the host matrix and enlarge the channel dimensions (Figs. 5e and f). The materials of $V_{10}O_{24}{\cdot}12H_2O$ with bilayer structure showed high specific energy of 88.5 Wh/kg with a high power density of 12247.8 W/kg [87].

Recently, lots of low-valent vanadium compounds with cations, such as $K_2V_6O_{16}{\cdot}2.7H_2O$ [88], $Na_2V_6O_{16}{\cdot}3H_2O$ [89], are promising cathodes for aqueous ZIBs. The $(NH_4)_2V_6O_{16}{\cdot}1.5H_2O$ synthesized by Lai *et al.* delivered a capacity of 268 mAh/g with 87% retained capacity after 1000 cycles at 5 A/g [90]. Alfaruqi's group [91] revealed the electrochemical mechanism of Zn ions insertion in LiV_3O_8. The inserted Zn ions occupied the sites of Li and the stoichiometric $ZnLiV_3O_8$ phase formed during the discharge process. With the progress of discharging process, continuous insertion of Zn ions led to the formation of $Zn_yLiV_3O_8$. During the charging process, the extraction of Zn ions promoted the recovery

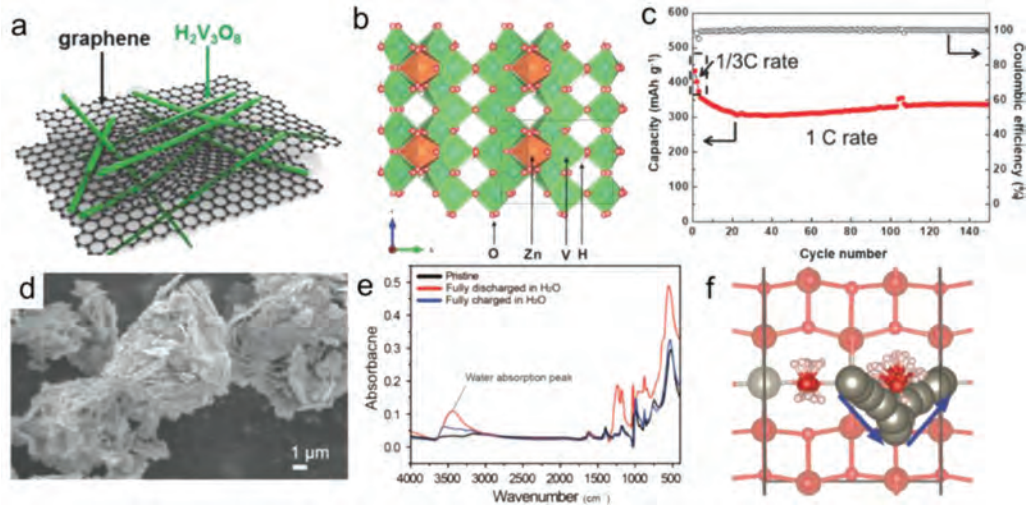

Fig. 5. (a) Schematic illustration, (b) crystal structure and (c) cycling performance of $H_2V_3O_8$/ graphene. Copied with permission [84]. Copyright 2018, Wiley-VCH. (d) SEM image, (e) *ex situ* FT-IR spectra and (f) kinetic behavior of Zn of V_6O_{13}. Copied with permission [86]. Copyright 2019, Wiley-VCH.

of the LiV_3O_8. The high reversibility contributed to a high capacity of 267 mAh/g at 16 mA/g. Wang and coworkers [92] synthesized $Ba_xV_3O_8$-type nanobelts with robust structures. Compared to $Ba_xV_2O_5{\cdot}nH_2O$, $Ba_xV_3O_8$ suppressed the cathode dissolution and eliminated the irreversible byproduct $Zn_4SO_4(OH)_6{\cdot}xH_2O$, leading to superior rate capability and long-term cyclic stability. Liu *et al.* [93] synthesized $CaV_6O_{16}{\cdot}3H_2O$ based on microwave reaction, and it was a typical vanadium-bronze mineral. The Ca ions were located in the interlayer space and coordinated by oxygens from the two vanadium slabs. Ca ions improved the interplanar spacing and the electrode material reversibly intercalated up to 4.5 equiv. of Zn ions per mole of $CaV_6O_{16}{\cdot}3H_2O$, delivering high specific capacity with excellent capacity retention. The preinsertion of dual cations into the V_3O_8 structure could benefit from the advantageous role of both monovalent and divalent cations. Zhu *et al.* [94] selected Na ions and Ca ions to pre-insert into V_3O_8 layer structure. The $NaCa_{0.6}V_6O_{16}{\cdot}3H_2O$ nanobelts showed excellent electrochemical performances: the original capacity reached 347 mAh/g at 0.1 A/g, and the capacity retention rate was 94% after 2000 cycles at 2 A/g.

It can be concluded that bring oxygen vacancy into Vanadium oxide layers can improve the battery performance in different ways. Intercalating cations can significantly enlarge the interlayer spacing and stabilize the structure, which can improve the specific capacity and electrochemical performance.

5. Vanadium-based composites with different morphologies

The past decade has witnessed the successful synthesis of cathode materials in a rich variety of morphologies used for ZIBs, which includes lamellar, linear, ribbon, spherical, *etc*. The shape not only controls its physicochemical properties but also determines its merit for electronic transmission. For example, the nanowires with ultra-long structure (Fig. 6a) and nanoplates with ultra-thin morphology (Fig. 6b) are favorable to provide a large contact area and shorten the ion diffusion path [45,85]. Liang *et al.* prepared hollow nanospheres consisted of nanoflakes (Fig. 6c), which provided more active sites and increased the ion diffusion ability (Fig. 6d) [95]. Some morphologies with micropores provided more ion diffusion ways [96,97]. As shown in Figs. 6e and f, the scroll shells were composed of 10~20 ultrathin layers (thickness of 2~3 nm) with the spaces of 1~3 nm between adjacent layers, which facilitated easy electrolyte penetration and enhanced the active sites [98]. Microspheres (Fig. 6g) and nanoflowers (Figs. 6h and i) create more pathways, resulting in high capacity [96,99–101]. These kinds of structures with a large specific surface area can supply more active sites, shorten the transmission channel of electrolyte ions, and have strong structural stability, which leads to superior electrochemical performance.

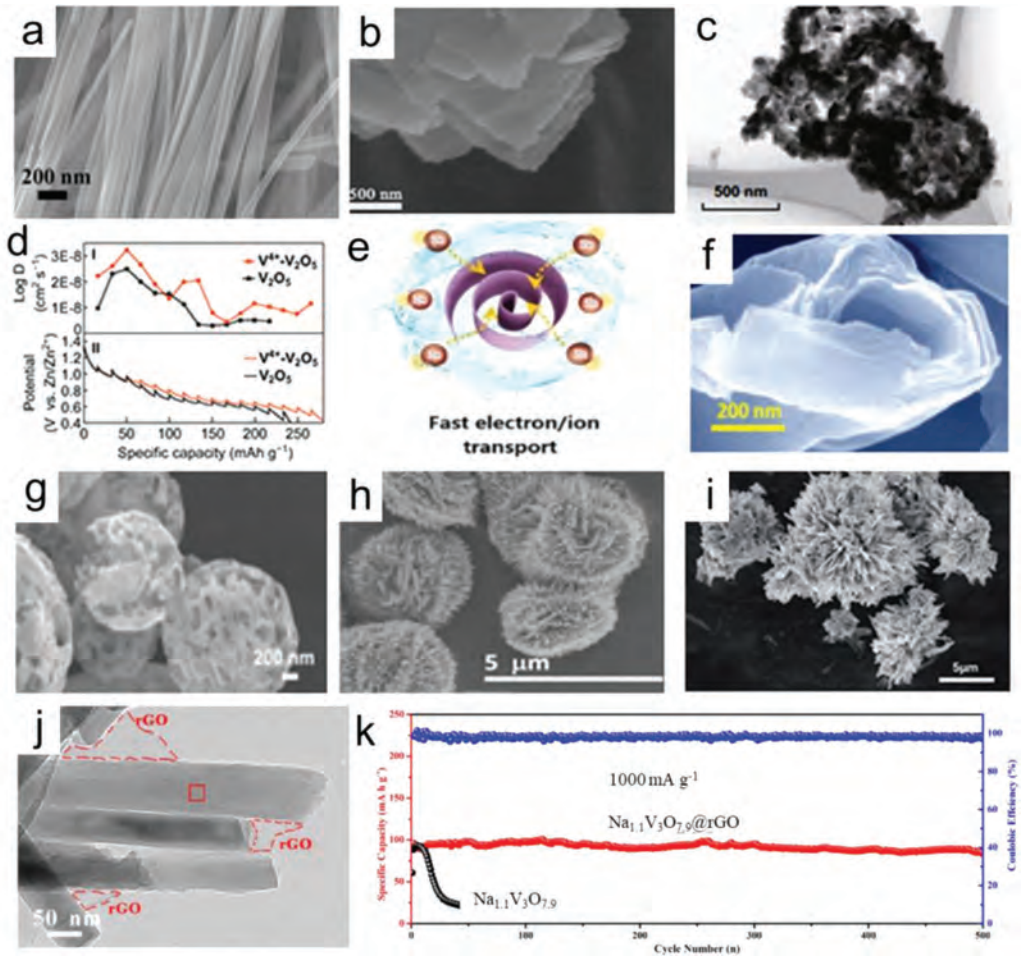

Fig. 6. (a) SEM of $Na_{0.33}V_2O_5$. Copied with permission [45]. Copyright 2018, Wiley-VCH. (b) SEM of V_6O_{13}. Copied with permission [85]. Copyright 2019, Wiley-VCH. (c) TEM and (d) GITT curves of V_2O_5 nanospheres. Copied with permission [95]. Copyright 2019, Springer. (e) Schematic image and (f) SEM of V_6O_{13}-δ@C nanoscrolls. Copied with permission [98]. Copyright 2020, Wiley-VCH. (g) SEM of V_2O_5 microspheres. Copied with permission [96]. Copyright 2019, the Royal Society of Chemistry. (h) SEM of MgV_2O_4 microsphere. Copied with permission [100]. Copyright 2020, ACS. (i) SEM of NaV_6O_{15}. Copied with permission [101]. Copyright 2020, the Royal Society of Chemistry. (j) TEM and (k) cycle performance of $Na_{1.1}V_3O_{7.9}$. Copied with permission [108]. Copyright 2018, Elsevier.

Many vanadium based materials suffers from poor electrical conductivity, which results in poor cycling performance and ionic transport kinetics. Graphene [102–105] and CNTs [106,107] modified cathode materials to stabilize the structure and improve conductivity by providing more efficient pathways for ion/electron transportation. Cai [108] prepared pilotaxitic $Na_{1.1}V_3O_{7.9}$ nanoribbons wrapped by graphene film through facial hydrothermal reaction. The existence of rGO provided modified electronic conductivity and the ability to buffer the variation of stress and volume during discharging/charging process (Fig. 6j). When it was used in aqueous ZIBs, the $Na_{1.1}V_3O_{7.9}$@rGO cathode demonstrated the satisfying electrochemical properties (Fig. 6k). In another literature, carbon and rGO were used together to improve the conductivity and enhance the electrochemical performance of $Na_3V_2(PO_4)_3$ [78]. The $Na_3V_2(PO_4)_3$ particles were distributed uniformly on the surface of rGO nanosheets. The rGO sheets enhanced the charge transfer *via* the interconnected conducting scaffolds and acted as the heterogeneous nucleation sites to facilitate the growth of $Na_3V_2(PO_4)_3$ particles. CNTs significantly boosted the electrochemical stability of V_2O_5, which has a capacity retention of 72% after 6000 cycles at 5 A/g [106]. CNTs could serve as the electron connecting network, which was beneficial to the Zn ions diffusion [109]. Compared to the pure V_2O_5, the composite film composed of carbon nanotube film and V_2O_5 (CNTF@V_2O_5) showed a super high and stable capacity. [110]. Z. Niu *et al.* prepared KV_3O_8•$0.75H_2O$ and further incorporated them into single-walled carbon nanotubes (SWCNTs) network, achieving freestanding KVO/SWCNTs composite films. The KVO/SWCNTs cathodes exhibited a Zn^{2+}/H^+ insertion/extraction mechanism, resulting in fast kinetics of ion transfer [111].

The architecture of nanostructure and carbon-based composite materials can provide more and shorter ion diffusion ways, reduce structural stress during cycles, improve the conductivity, and also reinforce the structure.

6. Summary and prospect

Recent years have witnessed great progress in exploiting vanadium-based aqueous ZIBs with regard to the synthesis, characterization, electronic structures and exceptional performances. They have shown excellent electrochemical properties due to the multivalence and layered structure. This review has outlined the various tactics to improve the properties of vanadium-based cathodes, including ions insertion, morphology adjustment, and carbon materials modification. The corresponding synthesis method, electrochemical performance and energy storage mechanism were also discussed.

Despite the tremendous achievements arising from the vanadium-based aqueous ZIBs in recent years, there are still several issues should be carefully considered for future design of more effective devices. In this section, the associated challenges are summarized and perspectives are also proposed, which was shown in Fig. 7.

(1) The energy storage mechanism of aqueous ZIBs is complex. The interlayer ions, crystal water, or oxygen vacancy may powerfully increase the lattice spacing and provide more ion diffusion ways with reduced kinetic potential energy for the diffusion of hydrous Zn ions. A quantitative understanding for the contribution of different factors in vanadium-based compounds to energy storage mechanism is still lacking for the operation process. Deep understanding for the microstructure evolution of the active material and the reaction mechanisms with the assistance of *in-situ* technology will beneficial for theoretical guidance for the rational design and application of aqueous ZIBs in the future.

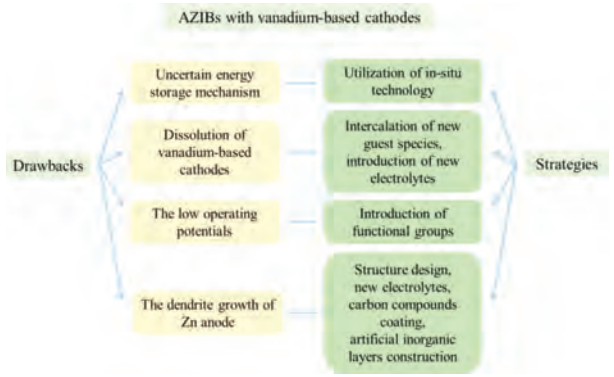

Fig. 7. Drawbacks and prospective strategies of aqueous ZIBs with vanadium-based cathodes.

(2) The unfortunate shortcoming of vanadium-based compounds is their solubility in water system electrolytes. A variety of vanadium oxide or vanadate always undergo detrimental dissolution, exfoliation, or shape degeneration, leading to the structure collapse and drastically change their cycling stability, which makes it difficult to realize large-scale commercial application. In order to successfully use vanadium-based compounds into future renewable energy systems, it is necessary to find new guest species to pre-intercalate into vanadium oxide layers as pillars and the suitable electrolytes.

(3) The discharge voltage platform of vanadium-based cathodes is relatively low, with usually poor energy density, which makes it difficult to realize efficient application. In order to successfully use vanadium-based cathodes into future renewable energy systems, it is necessary to utilize functional groups, such as PO_4^{3-}, F^- to increase the operating voltage and the energy density.

(4) The dendrite growth of Zn anode is still a challenge in aqueous ZIBs, which leads to the capacity fading and battery life degradation. Thus, it is urgently necessary to find new strategies such as designing the structure of Zn anode, changing suitable electrolytes, coating the vanadium-based compounds with the carbon or building artificial inorganic layers to inhibit the growth of Zn dendrite.

Declaration of competing interest

The authors declare that they have no known competing financial interests or personal relationships that could have appeared to influence the work reported in this paper.

Acknowledgments

This work was financially supported by the State Key Lab of Advanced Metals and Materials (No. 2020-Z14), the Startup Funds from the Henan University of Science and Technology (Nos. 13480095 and 13480096), the National Natural Science Foundation of China (No. 52002119).

References

[1] F. Duffner, N. Kronemeyer, J. Tübke, et al., Nat. Energy 6 (2021) 123–134.
[2] B. Liu, J.G. Zhang, W. Xu, Joule 2 (2018) 833–845.
[3] J. Tan, D. Li, Y. Liu, et al., J. Mater. Chem. A 8 (2020) 7980–7990.
[4] B. Dou, J. Yan, Q. Chen, et al., Sens. Actuator. B: Chem. 328 (2021) 129082.
[5] W. Shen, J. Zang, H. Hu, et al., Mater. Des. 195 (2020) 108992.
[6] H. Hu, Y. Hu, H. Cheng, et al., J. Power Sources 491 (2021) 229617.
[7] Y. Tian, G. Zeng, A. Rutt, et al., Chem. Rev. 121 (2021) 1623–1669.
[8] C. Guo, Q. Wang, J. He, et al., J. Phys. Chem. Lett. 11 (2020) 905–912.
[9] G. Harper, R. Sommerville, E. Kendrick, et al., Nature 575 (2019) 75–86.
[10] H. Hu, H. Cheng, K. Song, et al., J. Power Sources 472 (2020) 228599.

[11] Y. Yamada, J. Wang, S. Ko, et al., Nat. Energy 4 (2019) 269–280.
[12] S. Dai, Y. Bai, W. Shen, et al., J. Power Sources 482 (2021) 228915.
[13] D.H.S. Tan, A. Banerjee, Z. Chen, Y.S. Meng, Nat. Nanotechnol. 15 (2020) 170–180.
[14] J.Y. Hwang, S.T. Myung, Y.K. Sun, Chem. Soc. Rev. 46 (2017) 3529–3614.
[15] R. Rajagopalan, Y. Tang, X. Ji, et al., Adv. Funct. Mater. 30 (2020) 1909486.
[16] G. Fang, J. Zhou, A. Pan, et al., ACS Energy Lett. 3 (2018) 2480–2501.
[17] L. Zhang, L. Chen, X. Zhou, et al., Adv. Energy Mater. 5 (2015) 18263.
[18] H. Pan, Y. Shao, P. Yan, et al., Nat. Energy 1 (2016) 16039.
[19] C. Xu, B. Li, H. Du, et al., Angew. Chem. Int. Ed. 51 (2012) 933–935.
[20] F.W. Thomas Goh, Z. Liu, T.S.A. Hor, et al., J. Electrochem. Soc. 161 (2014) A2080–A2086.
[21] N. Zhang, F. Cheng, J. Liu, et al., Nat. Commun. 8 (2017) 405.
[22] Z. Liu, G. Pulletikurthi, F. Endres, ACS Appl. Mater. Interfaces 8 (2016) 12158–12164.
[23] D. Kundu, P. Oberholzer, C. Glaros, et al., Chem. Mater. 30 (2018) 3874–3881.
[24] Y. Cheng, L. Luo, L. Zhong, et al., ACS Appl. Mater. Interfaces 8 (2016) 13673–13677.
[25] X. Gao, H. Wu, W. Li, et al., Small 16 (2020) 1905842.
[26] W. Jiang, X. Xu, Y. Liu, et al., J. Alloys Compd. 827 (2020) 154273.
[27] H. Zhang, Q. Liu, J. Wang, et al., J. Mater. Chem. A 7 (2019) 22079–22083.
[28] X. Gao, H. Wu, W. Li, et al., Small 16 (2020) 1905842.
[29] Q. Zhao, X. Chen, Z. Wang, et al., Small 15 (2019) 1904545.
[30] J. Hao, J. Mou, J. Zhang, et al., Electrochim. Acta 259 (2018) 170–178.
[31] Y. Jiang, D. Ba, Y. Li, et al., Adv. Sci. 7 (2020) 1902795.
[32] G. Zampardi, F.La Mantia, Curr. Opin. Electrochem. 21 (2020) 84–92.
[33] G. Liu, H. Huang, R. Bi, et al., J. Mater. Chem. A 7 (2019) 20806–20812.
[34] B. Häupler, A. Wild, U.S. Schubert, Adv. Energy Mater. 5 (2015) 1402034.
[35] Q. Zhao, W.W. Huang, Z.Q. Luo, et al., J. Sci. Adv. 4 (2018) 1761–1771.
[36] Y. Liang, Y. Jing, S. Gheytani, et al., Nat. Mater. 16 (2017) 841–848.
[37] M.S. Chae, J.W. Heo, S.C. Lim, et al., Inorg Chem. 55 (2016) 3294–3301.
[38] W. Zhang, C. Zuo, C. Tang, et al., Energy Technol. 9 (2020) 2000789.
[39] H. Zhao, Q. Fu, D. Yang, et al., ACS Nano 14 (2020) 11809–11820.
[40] P.Y. Zavalij, M.S. Whittingham, J. Acta Cryst. (1999) 627–663.
[41] M. Yan, P. He, Y. Chen, et al., Adv. Mater. 30 (2018) 1703725.
[42] L. Chen, Y. Ruan, G. Zhang, et al., Chem. Mater. 31 (2019) 699–706.
[43] K. Zhu, T. Wu, S. Sun, et al., Energy Storage Mater. 29 (2020) 60–70.
[44] Y. Yang, Y. Tang, G. Fang, et al., Energy Environ. Sci. 11 (2018) 3157–3162.
[45] P. He, G. Zhang, X. Liao, et al., Adv. Energy Mater. 8 (2018) 1702463.
[46] P. Hu, T. Zhu, X. Wang, et al., Nano Lett. 18 (2018) 1758–1763.
[47] F. Hu, D. Xie, D. Zhao, et al., J. Energy Chem. 38 (2019) 185–191.
[48] M. Du, C. Liu, F. Zhang, et al., Adv. Sci. 7 (2020) 2000083.
[49] Y. Hao, S. Zhang, P. Tao, et al., Chem. Nano Mat. 6 (2020) 797–805.
[50] W. Zhang, C. Tang, B. Lan, et al., J. Alloys Compd. 819 (2020) 797–805.
[51] B. Tang, G. Fang, J. Zhou, et al., Nano Energy 51 (2018) 579–587.
[52] L. Li, S. Liu, W. Liu, et al., Nano-Micro Lett. 13 (2021) 34.
[53] S. Islam, M.H. Alfaruqi, D.Y. Putro, et al., J. Mater. Chem. A 7 (2019) 20335–20347.
[54] S. Guo, G. Fang, S. Liang, et al., Acta Mater. 180 (2019) 51–59.
[55] L. Shan, Y. Yang, W. Zhang, et al., Energy Storage Mater. 18 (2019) 10–14.
[56] X. Wang, B. Xi, Z. Feng, et al., J. Mater. Chem. A 7 (2019) 19130–19139.
[57] L. Xu, Y. Zhang, H. Jiang, et al., Colloids Surf. A 593 (2020) 9–16.
[58] T. Wei, Q. Li, G. Yang, et al., J. Mater. Chem. A 6 (2018) 20402–20410.
[59] B. Tang, J. Zhou, G. Fang, et al., J. Electrochem. Soc. 166 (2019) A480–A486.
[60] D. Kundu, B.D. Adams, V. Duffort, et al., Nature Energy 1 (2016) 16119.
[61] C. Xia, J. Guo, P. Li, et al., Angew. Chem. Int. Ed. 57 (2018) 3943–3948.
[62] W. Zhou, M. Chen, A. Wang, et al., J. Energy Chem. 52 (2021) 377–384.
[63] C. Patridge, J. Coord. Chem. 72 (2019) 1253–1266.
[64] F. Ming, H. Liang, Y. Lei, et al., ACS Energy Lett. 3 (2018) 2602–2609.
[65] N. Wang, C. Sun, X. Liao, et al., Adv. Energy Mater. (2020) 2002293.
[66] C. Liu, Z. Neale, J. Zheng, et al., Energy Environ. Sci. 12 (2019) 2273–2285.
[67] J. Li, K. McColl, X. Lu, et al., Adv. Energy Mater. 10 (2020) 2000058.
[68] Y. Yang, S. Liang, Z. Wu, et al., Nano Energy 61 (2019) 617–625.
[69] L. Shan, J. Zhou, M. Han, et al., J. Mater. Chem. A 7 (2019) 7355–7359.
[70] X. Yu, F. Hu, F. Cui, et al., Dalton Trans. 49 (2020) 1048–1055.
[71] Y. Liu, Q. Li, K. Ma, et al., ACS Nano 13 (2019) 12081–12089.
[72] J.H. Jo, Y.K. Sun, S.T. Myung, J. Mater. Chem. A 5 (2017) 8367–8375.
[73] C. Xia, J. Guo, Y. Lei, et al., Adv Mater. 30 (2017) 1705580.
[74] L. Chen, Z. Yang, J. Wu, et al., Electrochim. Acta 330 (2020) 135347.
[75] Z. Peng, Q. Wei, S. Tan, et al., Chem. Commu. 54 (2018) 4041–4044.
[76] G. Li, Z. Yang, Y. Jiang, et al., Nano Energy 25 (2016) 211–217.
[77] W. Song, Z. Wu, J. Chen, et al., Electrochim. Acta 146 (2014) 142–150.
[78] G. Li, Z. Yang, Y. Jiang, et al., J. Power Sources 308 (2016) 52–57.
[79] H.B. Zhao, C.J. Hu, H.W. Cheng, et al., Sci. Rep. 6 (2016) 25809.
[80] W. Li, K. Wang, S. Cheng, et al., Energy Storage Mater. 15 (2018) 14–21.
[81] Q. Ni, H. Jiang, S. Sandstrom, et al., Adv. Funct. Mater. 30 (2020) 2003511.
[82] D. Kundu, S. Hosseini Vajargah, L. Wan, et al., Energy Environ. Sci. 11 (2018) 881–892.
[83] P.J. Wang, X.D. Shi, Z.X. Wu, et al., Carbon Energy 2 (2020) 297–301.
[84] Q. Pang, C. Sun, Y. Yu, et al., Adv. Energy Mater. 8 (2018) 1800144.
[85] L. Shan, J. Zhou, W. Zhang, et al., Energy Technol. 7 (2019) 1900022.
[86] J. Shin, D.S. Choi, H.J. Lee, et al., Adv. Energy Mater. 9 (2019) 1900083.
[87] T. Wei, Q. Li, G. Yang, et al., Electrochim. Acta 287 (2018) 60–67.
[88] B. Sambandam, V. Soundharrajan, S. Kim, et al., J. Mater. Chem. A 6 (2018) 15530–15539.
[89] V. Soundharrajan, B. Sambandam, S. Kim, et al., Nano. Lett. 18 (2018) 2402–2410.
[90] J. Lai, H. Tang, X. Zhu, et al., J. Mater. Chem. A 7 (2019) 23140–23148.
[91] M.H. Alfaruqi, V. Mathew, J. Song, et al., Chem. Mater. 29 (2017) 1684–1694.
[92] Y. Cai, R. Chua, Z. Kou, et al., ACS Appl. Mater. Interfaces 12 (2020) 36110–36118.
[93] X. Liu, H. Zhang, D. Geiger, et al., Chem. Commu. (Camb) 55 (2019) 2265–2268.
[94] K. Zhu, T. Wu, K. Huang, Adv. Energy Mater. 9 (2019) 1901968.
[95] F. Liu, Z. Chen, G. Fang, et al., Nano-Micro Lett. 11 (2019) 25.
[96] P. Hu, T. Zhu, J. Ma, et al., Chem. Commu. 55 (2019) 8486–8489.
[97] R. Li, H. Zhang, Q. Zheng, et al., J. Mater. Chem. A 8 (2020) 5186–5193.
[98] Y. Lin, F. Zhou, M. Xie, et al., ChemSusChem 13 (2020) 3696–3706.
[99] Y. Ding, Y. Peng, W. Chen, et al., Appl. Surf. Sci. 493 (2019) 368–374.
[100] W. Tang, B. Lan, C. Tang, et al., ACS Sustainable Chem. Eng. 8 (2020) 3681–3688.
[101] R. Li, C. Guan, X. Bian, et al., RSC Adv. 10 (2020) 6807–6813.
[102] I.S. Chae, T. Luo, G.H. Moon, et al., Adv. Energy Mater. 6 (2016) 5607–5615.
[103] G. Xu, X. Liu, S. Huang, et al., ACS Appl. Mater. Interfaces 12 (2020) 706–716.
[104] S. Wang, K. Zhu, L. Yang, et al., Ionics (Kiel) (2020) 25446–25453.
[105] C. Shen, X. Li, N. Li, et al., ACS Appl. Mater. Interfaces 10 (2018) 25446–25453.
[106] H. Chen, H. Qin, L. Chen, et al., J. Alloys Compd. 842 (2020) 155912.
[107] R. Venkatkarthick, N. Rodthongkum, X. Zhang, et al., ACS Appl. Energy Mater. 3 (2020) 4677–4689.
[108] Y. Cai, F. Liu, Z. Luo, et al., Energy Storage Mater. 13 (2018) 168–174.
[109] Y. Li, Z. Huang, P.K. Kalambate, et al., Nano Energy 60 (2019) 752–759.
[110] X. Wang, L. Wang, B. Zhang, et al., J. Energy Chem. 59 (2021) 126–133.
[111] F. Wan, S. Huang, H. Cao, et al., ACS Nano 14 (2020) 6752.